

PAPER • OPEN ACCESS

Plasmon-assisted polarization-sensitive photodetection with tunable polarity for integrated silicon photonic communication systems

To cite this article: Zehao Song *et al* 2021 *Nanotechnology* **32** 505205

View the [article online](#) for updates and enhancements.

You may also like

- [2D semiconductors towards high-performance ultraviolet photodetection](#)
Qi Zhang, Xin Li, Zhiwei He *et al.*
- [Light-matter interaction of 2D materials: Physics and device applications](#)
Zi-Wei Li, , Yi-Han Hu *et al.*
- [Hot electron photodetection with spectral selectivity in the C-band using a silicon channel-separated gold grating structure](#)
Hongbin Xiao, Shu-Cheng Lo, Yi-Hsin Tai *et al.*



IOP | ebooks™

Bringing together innovative digital publishing with leading authors from the global scientific community.

Start exploring the collection—download the first chapter of every title for free.

Plasmon-assisted polarization-sensitive photodetection with tunable polarity for integrated silicon photonic communication systems

Zehao Song^{1,3} , Masiar Sistani^{1,3} , Lukas Wind¹, Darius Pohl², Bernd Rellinghaus², Walter M Weber¹ and Alois Lugstein¹ 

¹Institute of Solid State Electronics, Technische Universität Wien, Gußhausstraße 25-25a, A-1040 Vienna, Austria

²Dresden Center for Nanoanalysis, cfaed, Technische Universität Dresden, Helmholtzstraße 18, Dresden D-01069, Germany

E-mail: alois.lugstein@tuwien.ac.at

Received 21 July 2021, revised 9 September 2021

Accepted for publication 20 September 2021

Published 6 October 2021



CrossMark

Abstract

To establish high-bandwidth chip-to-chip interconnects in optoelectronic integrated circuits, requires high-performance photon emitters and signal receiving components. Regarding the photodetector, fast device concepts like Schottky junction devices, large carrier mobility materials and shrinking the channel length will enable higher operation speed. However, integrating photodetectors in highly scaled ICs technologies is challenging due to the efficiency-speed trade-off. Here, we report a scalable and CMOS-compatible approach for an ultra-scaled germanium (Ge) based photodetector with tunable polarity. The photodetector is composed of a Ge Schottky barrier field effect transistor with monolithic aluminum (Al) source/drain contacts, offering plasmon assisted and polarization-resolved photodetection. The ultra-scaled Ge photodetector with a channel length of only 200 nm shows high responsivity of about $R = 424 \text{ A W}^{-1}$ and a maximum polarization sensitivity ratio of $\text{TM/TE} = 11$.

Supplementary material for this article is available [online](#)

Keywords: photodetector, negative photoconductivity, photogating effect, polarization sensitivity, plasmon-assisted photodetection

(Some figures may appear in colour only in the online journal)

1. Introduction

In the post-Moore era, optoelectronic integrated circuits (OEICs) are considered as a promising scheme for overcoming

limitations of electrical and thermal parasitics associated with MOS scaling [1, 2]. In the context of the development of high-performance photodetectors required for this purpose, Ge has once again moved into the center of interest. Owing to the excellent optoelectronic properties, which include high responsivity [3] from visible to near-infrared wavelengths, high bandwidths [4] and compatibility with CMOS fabrication, Ge on silicon based devices may become an integral part of next generation integrated silicon photonic communication systems. However, while advanced field effect transistors have already been downscaled to a few nanometers [5], the common

³ These authors contributed equally to this work.



Original content from this work may be used under the terms of the [Creative Commons Attribution 4.0 licence](#). Any further distribution of this work must maintain attribution to the author(s) and the title of the work, journal citation and DOI.

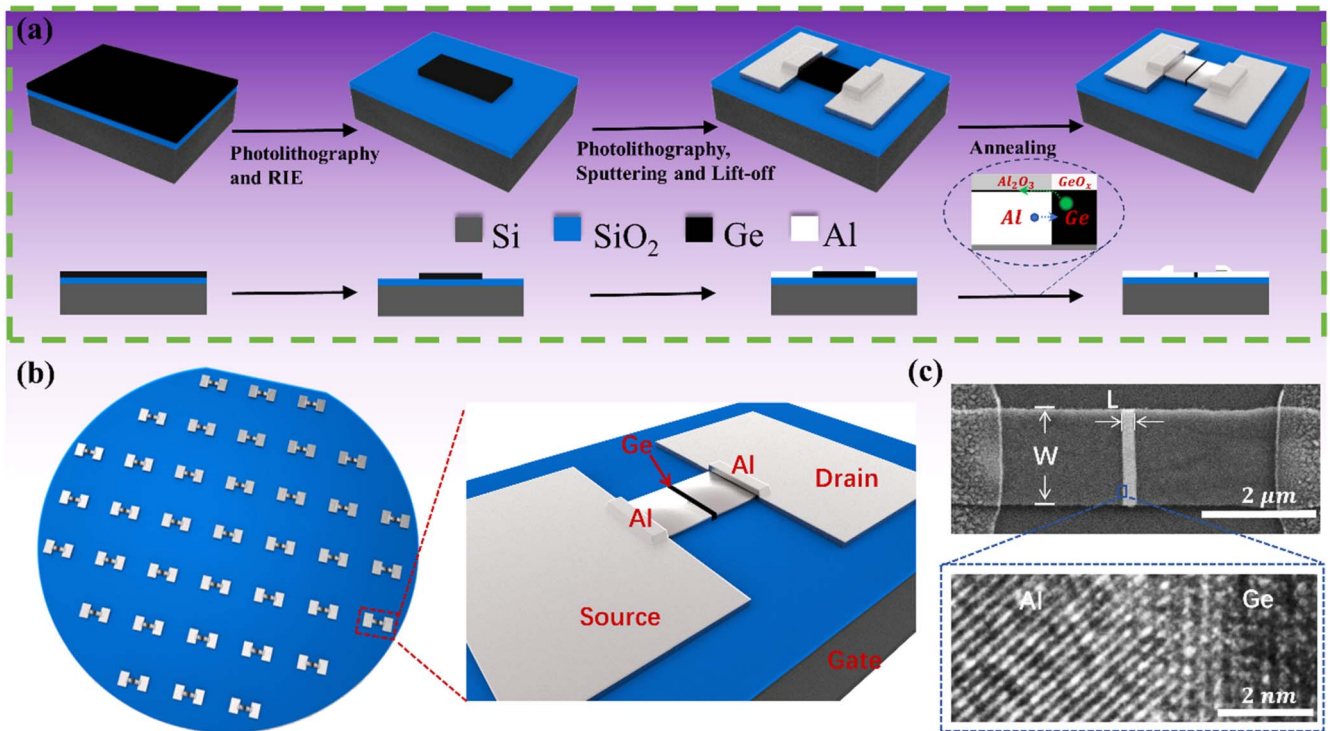


Figure 1. Device fabrication scheme. (a) Schematic diagram of the fabrication process based on a GeOI wafer substrate. The inset depicts the mechanism of the Al–Ge exchange via rapid thermal annealing for heterostructure formation. (b) Diagram of the wafer-scale Al–Ge–Al device array. The enlarged panel shows the detail view of the Ge SBFET with two Al pads as source and drain electrodes and the Si handle wafer as common back gate. Corresponding microscope images are shown in (c). The upper panel shows the SEM image of a photodetector with a channel length of $L = 200$ nm and below the corresponding HRTEM image at the Al/Ge interface. The width and length of Ge channel are labelled as W and L in the upper panel, respectively.

dimension of a pixel of an imaging charged-coupled photodetection device still sticks on the micrometer scale [6], which causes integration mismatch and thus limits practical applications. The main challenge of scaling photodetectors even below the diffraction limit is the resulting low responsivity also regarded as the efficiency-speed trade-off [7, 8]. To meet higher operation speed and low-power requirements for high-bandwidth-density chip-to-chip interconnects, the photodetector must exhibit a low capacitance while attaining high responsivity. To overcome this limitation, one approach is utilizing the light concentrating properties of metallic nanostructures [9–11]. Thus, it has been demonstrated that redesigning electrodes as an optical antenna can enhance the sensitivity of a photodetector [12] and in the case of Ge, efficiently increase light absorption [11]. Further, well-designed plasmonic metal gratings offer the possibility of polarization-resolved photodetection [13, 14]. However, from the application perspective both, detection performance and fabrication issues have to be considered. Most of the proposed plasmon-assisted photodetectors employ III–V compound semiconductors and gold as the metal due to its chemical inertness [15]. Apart from the fact that these are cost-intensive materials, they are difficult to integrate into mature Si platform technology. In this regard, it is of particular interest that Al plasmonic gratings have been confirmed to have the capability of enhancing light absorption even in the visible spectrum [16]. In this letter, we demonstrate a scalable approach for an ultra-scaled, CMOS-compatible Ge Schottky barrier

device with monolithic Al electrodes for plasmon-assisted photodetection, with high responsivity. The electrostatically tunable polarity and polarization sensitivity measurement offered by this device will further enhance the information bandwidth in optoelectronic integrated circuits.

2. Results and discussion

Figure 1(a) illustrates the wafer-scale fabrication scheme of the monolithic metal–semiconductor–metal (Al–Ge–Al) photodetector. First of all, Ge pads are patterned from an intrinsic Ge on insulator (GeOI) wafer using optical lithography and reactive-ion etching (RIE). Thereafter Al contacts are attached to the Ge pads using again optical lithography, Al sputter deposition and lift-off techniques. The photosensitive detector area is hereafter adjusted by controlling the Ge channel length via a thermal induced Al–Ge exchange reaction, of which mechanism is basically illustrated in the inset of figure 1(a) and discussed in detail in our former works [17, 18]. Such standard semiconductor processing enables the wafer-scale fabrication (figure 1(b)) of arrays of ultra-scaled devices with a reproducible channel length even below 50 nm [19]. The scanning electron microscopy (SEM) image in figure 1(c) shows a typical Al–Ge–Al heterojunction device with a Ge channel length of $L = 200$ nm and a height of 75 nm, determined by the intrinsic device layer thickness of the GeOI

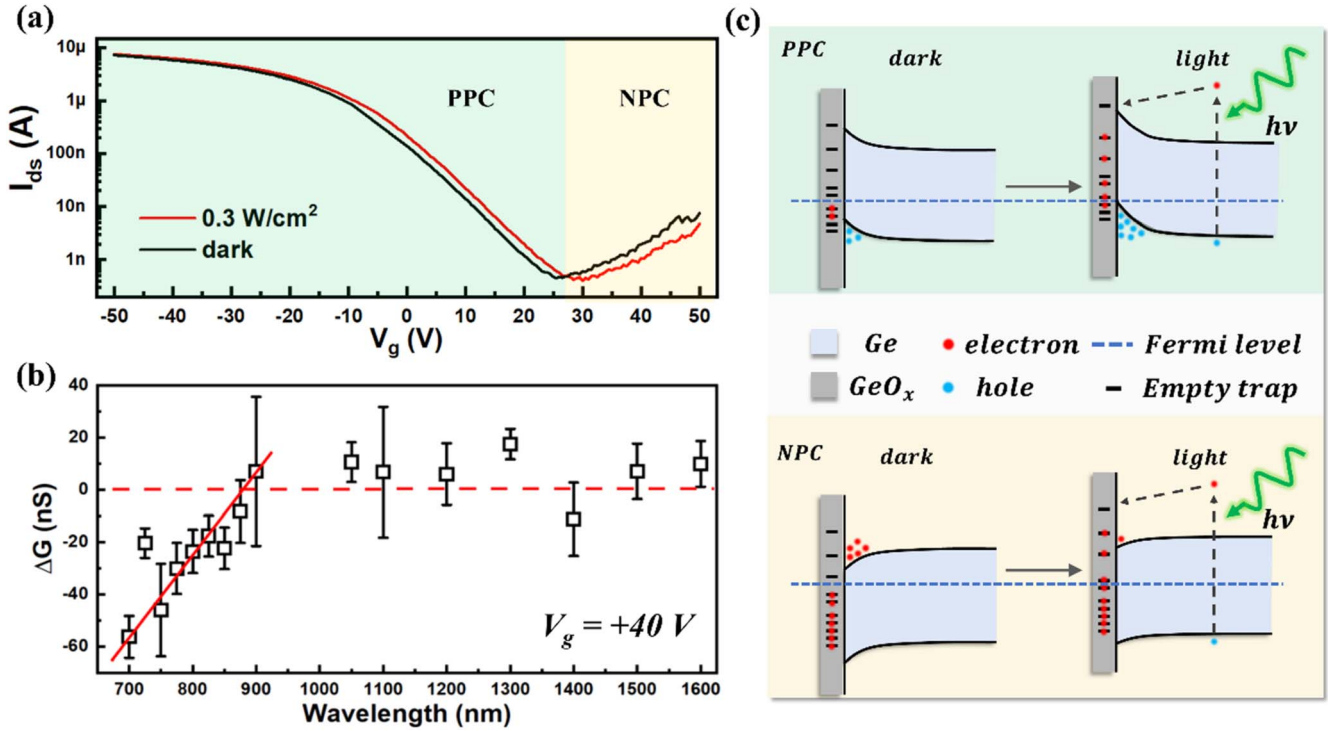


Figure 2. Tunable photoconductivity. (a) Transfer characteristic of a Ge SBFET with a channel length of $L = 200$ nm with and without illumination ($\lambda = 532$ nm) with a laser intensity of 0.3 W cm^{-2} . The drain voltage was set to 10 mV. (b) Photoconductance $\Delta G = G_{\text{ph}} - G_{\text{d}}$, as a function of wavelength. The error bars are the standard deviation of experimental values from 5 repeating measurements. (c) Band diagrams for a descriptive discussion of PPC and NPC.

wafer. Without limiting the generality the Ge channel width of all devices within this investigations was chosen with $W = 2 \mu\text{m}$. Besides the possibility of parallel processing this approach enables ultra-scaled metal–semiconductor–metal devices with remarkable abrupt Al–Ge interfaces (see high resolution transmission electron microscopy (HRTEM) image in figure 1(c)) with low contact resistance [17]. Such monolithic Al–Ge–Al heterostructures on the GeOI wafer resemble back-gated Schottky barrier field-effect transistors (SBFETs) with the 120 nm thick buried silicon oxide acting as gate dielectric and the handle wafer as common back gate (figure 1(b)).

Figure 2(a) shows a typical transfer ($I_{\text{ds}}-V_{\text{g}}$) characteristics of an Al–Ge–Al SBFET with a channel length of $L = 200$ nm and a width of $W = 2 \mu\text{m}$ in dark and under laser irradiance ($\lambda = 532$ nm) of 0.3 W cm^{-2} , respectively. Without illumination the device behaves like a p-channel enhancement mode transistor with the characteristic sharp increase in drain current for negative gate voltages. Notably, this p-type behavior is not a result of unintentional Al doping of the Ge channel during the Al/Ge exchange, but commonly observed for unpassivated Ge based devices due to effective surface doping [20]. For the actual 75 nm thick Ge channel, surface states at the GeO_x/Ge interface and negatively charged traps in the native oxide determine the electronic response with holes as majority carriers [21]. Such trap states with time constants up to several minutes [20] induces also inevitable hysteresis phenomena in the double-sweeping transfer characteristics (figure S1(a) (available online at stacks.iop.org/

NANO/32/505205/mmedia)) due to a delayed response on abrupt changes of the gate voltages (figure S1(b)). For the actual Ge SBFET, scattering at charged surface traps also leads to a significant reduction of the carrier mobility to approximately $445 \text{ cm}^2 \text{ V}^{-1} \text{ s}^{-1}$ (suppl. information—figure S1(a)) in agreement with other reports on GeOI wafer-based devices [22]. However, as the gate voltage increases, hole accumulation decreases and, after depletion of charge carriers, inversion occurs for sufficiently large positive gate voltages, the current of which is dominated by electrons.

Under laser irradiance the overall shape of the transfer characteristic remains essentially the same, but somewhat shifted towards more positive gate voltages. This shift of the threshold voltage is reflected in an increase of the drain current in the hole accumulation and depletion regime, commonly depicted as positive photoconductivity (PPC) (area highlighted green in figure 2(a)). Since the energy of the exciting photons (2.33 eV) is far above the bandgap of Ge, photogenerated hot electrons efficiently fill the, above mentioned, localized surface states and traps. These now negatively charged traps localized in close proximity to the current-carrying channel of the SBFET act as a very effective local gate and cause the observed shift in threshold voltage. The photogating effect can be expressed by [23]

$$I_{\text{ph}} \approx g_m \cdot \Delta V_{\text{th}}, \quad (1)$$

where I_{ph} is the photocurrent, $g_m = dI_{\text{ds}}/dV_{\text{g}}$ is the transconductance and ΔV_{th} the irradiation induced shift of the threshold voltage. The effect of photogating is even more

tangible at high light intensities (figure S2) and leads to impressively high responsivity, gain and detectivity of $R = 424 \text{ A W}^{-1}$, $g = 1.4 \times 10^3$ and $D = 2 \times 10^{10}$ Jones, respectively determined at a gate voltage of $V_g = -50 \text{ V}$ under laser irradiance of 0.3 W cm^{-2} and a wavelength of $\lambda = 532 \text{ nm}$. Their dependence on the light intensity is shown and discussed in the supplementary (figure S3). Unfortunately, the photogating effect also leads to a significant limitation of the unpassivated Ge SBFET photodetector with regard to its temporal behaviour with rise and fall times of $\tau_{\text{rise}} = 1.07 \text{ s}$ and $\tau_{\text{fall}} = 1.2 \text{ s}$, respectively (figure S4). With respect to its use at different wavelengths, the Ge SBFET device shows pronounced PPC and high responsivity in the visible and near-infrared region (see figure S5) with cut-off near 1580 nm , in agreement with the bandgap of Ge.

Contrary in the electron dominated transport regime ($V_g > 27 \text{ V}$; area highlighted yellow in figure 2(a)) laser irradiance leads to a reduction of I_{ds} from now on referred to as negative photoconductivity (NPC). Thus, the responsivity and even the polarity of the photodetector can be adjusted only by changing the gate voltage. For the Ge SBFET device, NPC is observed when the Ge channel is in inversion behaving like an n-type semiconductor. Essentially, there are two mechanisms that can cause NPC in n-type semiconductors: (i) severe carrier scattering at photogenerated recombination centers [24] or (ii) trapping of photogenerated hot electrons inducing subsequently depletion of the conduction channel [25–27]. For the actual device, increased scattering seems to play a minor role, as the mobility remains largely unaffected, confirmed by the equal slope in the linear region of the transfer curves even for very high light intensities (figure S2). Meanwhile, photogenerated hot electrons fill up surface traps, making them negatively charged and thus by counteracting the positive back gate, lower the effective gate voltage applied to the Ge channel [26]:

$$V_g^{\text{eff}} = V_g - \frac{|Q_{\text{trap}}|}{C}, \quad (2)$$

where V_g is the applied gate voltage, Q_{trap} the charge of the filled surface traps and C the capacitance of the surface oxide.

The energy dependence of the occupation of the traps will be discussed briefly with reference to figure 2(b). Therefore, the photoconductance defined as $\Delta G = G_{\text{ph}} - G_{\text{d}}$ (where G_{ph} and G_{d} are the conductance of the Ge SBFET under illumination and at dark, respectively) is determined in the regime of NPC at $V_g = 40 \text{ V}$ at various wavelength. Starting at $\lambda = 700 \text{ nm}$, the photoconductance of $\Delta G = -60 \text{ nS}$ increases continuously with the wavelength until it finally levels off at around $\lambda = 900 \text{ nm}$ which corresponds to an energy of 1.34 eV . Accordingly, under the given biasing conditions, NPC due to photogating is observed only for light with an energy above 1.34 eV , indicating an equivalent activation barrier to fill the traps.

The effect of the traps on the polarity of the photoresponse will be shortly summarized with the help of the schematic band diagrams shown in figure 2(c). At negative gate voltages and without illumination, the Fermi level approximates the valence band and only traps below the Fermi level are filled. These, acting as an additional negative local gate, induce a further upward bending of the Ge bands and hence hole accumulation,

causing the common p-type like behavior of an unpassivated Ge channel. Upon irradiation with photons with sufficiently high energy, photogenerated hot electrons occupy traps above the Fermi level and thus reinforce the negative local gate. This is accompanied by an increased upward bending of the bands, which in turn leads to an increased accumulation of holes and thus improved conductivity resulting in the observed PPC.

At high positive gate voltages i.e. the regime where NPC is observed, the Fermi level is shifted towards the conduction band, which leads to downward bending of the conduction band, and thus accumulation of electrons at the interface. Notably the raised Fermi level already leads to increased occupation of traps near the edge of the conduction band, even without illumination. Under laser irradiance, further traps far above the Fermi level are filled by photogenerated high energetic electrons. These now negatively charged traps counteract the positive back gate, thus depleting electrons in the channel, which finally manifests itself in the observed NPC.

With the photogeneration of hot electrons being proportional to the light intensity and the overall number of traps limited, saturation of the photogating effect can be expected for high light intensities. Figure 3(a) shows the photoconductance of Ge SBFETs with different channel lengths as a function of the light intensity. The gate voltage was set to $V_g = +50 \text{ V}$ and the drain voltage adjusted to the different channel lengths so that the same field strengths of $E = 500 \text{ V cm}^{-1}$ prevail in all devices. For the device with a channel length of $L = 200 \text{ nm}$ one can clearly see the flattening of the NPC at approximately 6 W cm^{-2} and for all 3 devices even a change to PPC was observed for high light intensities. According to the hot carrier trapping model from *Y. Yang et al* [25], the photoconductivity i.e. light induced change of conductivity $\Delta\sigma$ at low light intensity can be derived as (suppl. information—figure S6)

$$\Delta\sigma = (\Delta n + n_{\text{hot}})e\mu_n = g e \mu_n \left(\tau_{\text{rec}} - \frac{\tau_{\text{th}} \tau_{\text{detrap}}}{\tau_{\text{trap}}} \right) \quad (3)$$

with Δn the density of electrons at the band-edge, n_{hot} the density of hot electrons, e the elementary charge, μ_n the mobility of electrons, g the photoexcitation rate, τ_{rec} the band-edge carrier recombination lifetime and τ_{th} , τ_{detrap} , τ_{trap} the hot carrier thermalization, detrapping and trapping time, respectively. The hot carrier thermalization time τ_{th} of Ge is reported in scale of picoseconds [28]. As mentioned above, the detrapping time of oxide states τ_{detrap} may take several minutes [29], whereas the trapping time of Ge is in the order of $\tau_{\text{trap}} = 10^{-7} - 10^{-8} \text{ s}$ [30]. Thus for low light intensities $\frac{\tau_{\text{th}} \tau_{\text{detrap}}}{\tau_{\text{trap}}}$ is larger than $\tau_{\text{rec}} = 10^{-3} \text{ s}$, which is the longest lifetime of electrons in Ge reported [31], resulting in NPC.

At high light intensity, practically all traps are filled up due to the long detrapping time and $\Delta\sigma$ becomes

$$\Delta\sigma \approx e\mu_n (g\tau_{\text{rec}} - N_{\text{trap}}). \quad (4)$$

The number of photons absorbed per second for the actual experimental setup are calculated to be more than 10^{11} for the highest light intensity of $P = 30 \text{ W cm}^{-2}$ (see suppl. information). Assuming a recombination lifetime of electrons

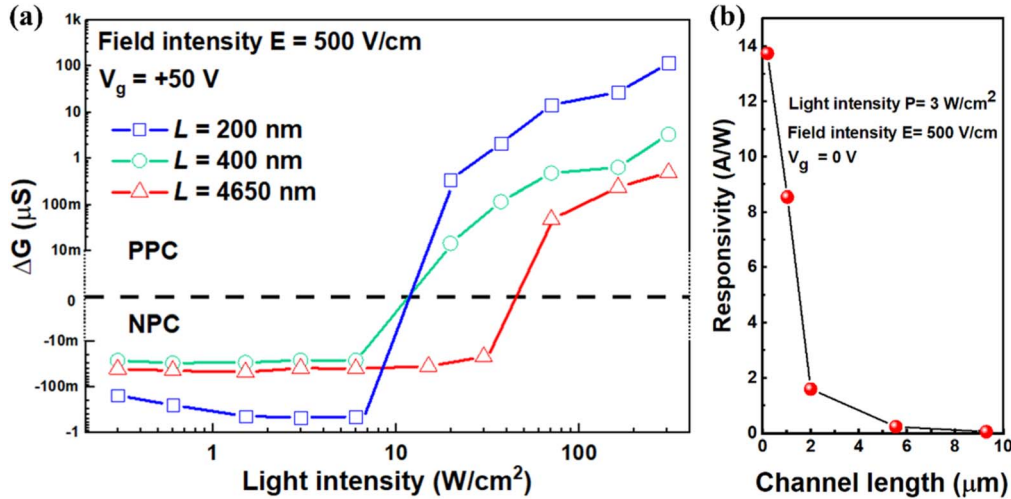


Figure 3. Photoconductance of devices with different channel lengths (a) ΔG of three devices with various channel lengths as the function of the light intensity at a gate voltage of $V_g = 50$ V. The bias voltage was adjusted accordingly to have the same electric field strength of $E = 500$ V cm^{-1} in all devices. (b) Responsivity as a function of channel length at a gate voltage of $V_g = 0$ V. All devices are measured at light intensity of 3 W cm^{-2} and an electric field intensity of 500 V cm^{-1} .

in the order of $\tau_{rec} = 10^{-4}$ s in n-type Ge with doping density of 10^{13} cm^{-3} [32], $g\tau_{rec}$ (in the scale of 10^7) is larger than N_{trap} (in the scale of 10^6 for a 200 nm channel device) resulting in an increase of photoconductivity. Thus for very high light intensities saturation of the traps rules out NPC as shown in figure S6. For all three devices we observed NPC at low light intensity turning to PPC at high light intensity, with the shortest channel device showing by far the strongest photoresponse for both NPC and PPC.

As operating a photodetector with gate voltages of a few tens of volts is not conceivably for practical applications we investigated ungated devices of various channel lengths, notably again with appropriate biasing to adjust the same field strength of $E = 500$ V cm^{-1} . Note that the choice of a thinner buried silicon oxide or a top-gated devices architecture with high- k dielectric could significantly reduce the required gate voltage. However the respective responsivity of the actual ungated device as a function of channel length shown in figure 3(b) is a measure of optical-to-electrical conversion efficiency and is given by:

$$R = \frac{I_{ph}}{S \cdot P} = \frac{I_{ph}}{W \cdot L \cdot P} \quad (5)$$

with I_{ph} the photocurrent, P applied light intensity and the area S ($S = W \cdot L$) of the photosensitive Ge segment. Somewhat surprising at first glance, the responsivity of the photodetector increases inversely proportional with the channel length of the Ge SBFET from $R = 6$ mA W^{-1} to $R = 13.7$ A W^{-1} when the photoactive Ge channel length scales down from $L = 9$ μm to $L = 200$ nm. In other words reducing the effective detector area by a factor of 45 results in an almost 240-fold enhancement of responsivity. Remarkably, this reinforcement is especially evident for ultra-scaled detectors with extremely short channel length even below the wavelength of $\lambda = 532$ nm, which is very promising in terms of the efficiency-speed trade-off. In accordance with other reports [11, 12], this responsivity enhancement in the M–S–M heterostructure device is attributed

to plasmon-assisted photodetection. The nanoscale monolithic Al electrodes which are assembled self-aligned during the thermal induced Al–Ge exchange reaction (see SEM image in figure 1(c)) reinforce the electromagnetic field intensity near its surrounding, enhancing light absorption and thus responsivity [33]. In addition, the photogenerated electron–hole pairs can be extracted more effectively in a shorter device and are therefore less likely to recombine.

Previous studies have further shown that metallic gratings can also introduce polarization-dependent functionality if their periods are less than the wavelength of the incident light [34–38]. Thus for ultra-scaled Ge SBFET devices the optical resonances of the nanoscale monolithic electrodes offer the ability to control the detector's polarization-dependent response [12, 39, 40], which may efficiently extend the information bandwidth in OEICs. Figure 4(a) shows a polarization-dependent photocurrent mapping for the ultra-scaled device with a channel length of $L = 200$ nm where φ defines the orientation of the polarization plane in relation to the Ge segment. It can be seen that the device provides the strongest response with the electric field oriented perpendicular (TM) to the Al–Ge interface (see figure 4(b)). The photocurrent of the device under TM incidence is about ~ 1.5 times greater than for TE incidence and the magnitude of photocurrent at a drain voltage of $V_{ds} = 10$ mV can be well fitted with a sinusoidal function (figure S7). As shown in the lower inset of figure 4(b) the Ge segment in this ultra-scaled Ge SBFET device appears as an elongated or nanowire-like structure about 2 μm long, 200 nm wide and only 75 nm thick. The highest photocurrent observed for TM incidence, is in contradiction to the polarization sensitivity of regular semiconductor nanowires which, due to the dielectric mismatch effect [41], show the highest photoresponse when light is polarized along their axis. The polarization dependence is thus a further evidence of the plasmon-assisted detection mechanism of the heterostructure M–S–M photodetector. The surface plasmon polariton resonance in the metal cavity

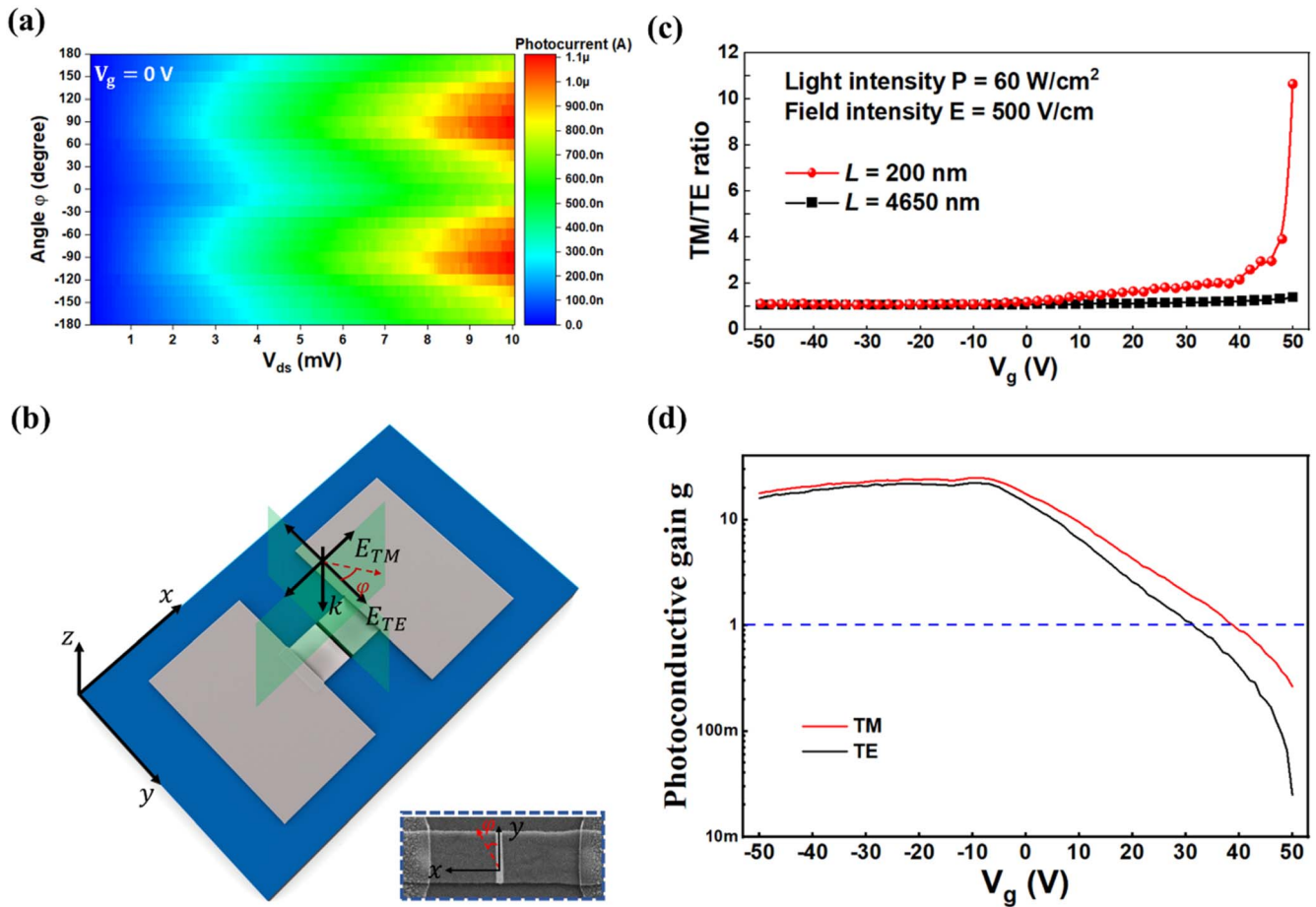


Figure 4. Polarization sensitivity of photodetector with a channel length of 200 nm. (a) Polarization dependent photocurrent mapping at positive drain bias. The gate voltage V_g and power density are set as 0 V and 30 W cm^{-2} , respectively. (b) A 3D diagram of the polarization angle-dependent photodetector. E_{TE} and E_{TM} present the direction of the electric field for TE and TM incidence, respectively. The inset shows the orientation of the polarization plane in relation to the Ge segment. (c) Gate dependent TM/TE ratio for an ultra-scaled ($L = 200$ nm) and rather long device ($L = 4650$ nm) under light irradiance of 60 W cm^{-2} at an electric field intensity of 500 V cm^{-1} . (d) the corresponding photoconductive gain of the ultra-scaled device ($L = 200$ nm) for TM and TE polarized light irradiance.

formed by the Al contacts can only effectively be driven with the electric field polarized normal to the M–S interface (i.e. TM direction) [42].

The polarization sensitivity appeared to be also critically dependent on the gate voltage due to the interplay of the regular photoelectric and photogating effect. Figure 4(c) shows the TM/TE ratio at a light intensity of 60 W cm^{-2} where we observe PPC within the whole range of the applied gate voltages (see figure S6). For the 200 nm long SBFET device, at negative gate voltages it shows overall high gain (figure 4(d)) with the TM/TE ratio close to one. Regardless of the polarization direction, the photoinduced hot electrons lead to a complete filling of all traps. As shown above these negatively charged traps act as an effective gate inducing a photoresponse with the gain of 20 (figure 4(d)). The TM/TE ratio increases steadily with the gate voltage to the maximum of TM/TE = 11 for the highest applicable gate voltage of 50 V. To the best of our knowledge this is the highest TM/TE ratio reported for Ge based photodetectors so far [43, 44]. For such high positive gate voltages the photocurrent mainly originates from regular photoelectric effect with a maximum gain of one when all photons are transferred to charge carriers

that are collected at either terminal before recombination. Photogating is also active at positive gate voltages, however, the negatively charged traps here block the electron transport in the channel. Thus in this regime we measure the intrinsic TM/TE ratio of the plasmon-assisted Ge SBFET detector. As expected, for longer devices, with Al contacts widely separated from each and thus not supporting plasmonic resonances, the TM/TE ratio appears to be widely independent from the gate voltage. For the device with a channel length of $L = 4650$ nm we determined a TM/TE ratio of about 1 over the entire accessible gate voltage range (figure 4(c)).

3. Conclusions

In conclusion, we have demonstrated an ultra-scaled plasmon-assisted Ge photodetector based on GeOI with monolithic Al contacts. The well controlled formation of Ge SBFET devices on a wafer-scale aside of lithographic limitations allows for a rational design for ultrascaled photodetectors with a high responsivity. We refined previous models developed for photogating effects in Ge based detectors enabling to control

initially thought detrimental effects of charge trapping to enhance responsivity. The monolithic Al electrodes that support plasmonic resonances in ultra-scaled devices result in a favourable redistribution in the electric fields that further enhances photocurrent, which is very promising in terms of the efficiency-speed trade-off. The polarity and polarization sensitivity of these three terminal device can be controlled electrostatically by the gate voltage thus providing more available states in OEICs to transit or store information. Thus, this work opens up a promising path of fabricating photo-detectors with the capability of enhancing information bandwidth in OEICs.

4. Methods

4.1. Device fabrication

The GeOI wafer used for device fabrication comprises a 75 nm thick (100)-oriented Ge device layer atop of a 150 nm buried SiO₂ layer and a 500 μm thick highly p-doped Si handle wafer. First of all, Ge nanosheets with the size of 10 μm × 2 μm were obtained by patterning the GeOI wafer using photolithography and RIE. Next step is to fabricate Al pads that overlap the ends of the Ge nanosheets on the SiO₂. These pads were defined again by photolithography followed by 100 nm Al sputtering and lift-off techniques. Prior to the Al deposition, a 5 s HI (14%) dip was performed for native GeO_x removal. Rapid thermal annealing at 674 K in forming gas (10% H₂/90% N₂) atmosphere was applied to initiate the Al-Ge exchange forming a monolithic Al-Ge-Al heterostructure. Finally, the back side of the sample was glued to a copper (Cu) plate by silver (Ag) paste to achieve a reliable back gate contact.

4.2. SEM and TEM measurements

The SEM images were carried out by the scanning electronic imaging function of an ion microscope (FEI Helios Nanolab 660). The same machine was also applied to prepare samples for HRTEM measurements via the focused ion beam lift-out function. HRTEM images are obtained from a FEI Titan3 80–300 image-corrected microscope.

4.3. Electrical/optical characterization

To survey photodetection performances under irradiance, a frequency doubled Nd:YAG laser emitting polarized light at λ = 532 nm was integrated into the system as the excitation source for light intensity-dependent and polarization-dependent measurement. The output power of the Nd:YAG laser could be adjusted from 0.1 μW to 10 mW. For the spectral measurement, another NKT SuperK Extreme laser with a monochromatic system (NKT SuperK Select acoustic-optical tunable filter (AOTF)) replaced the Nd:YAG laser as new monochromatic light source with the range from 500 nm to 1600 nm. A Zeiss 4X objective (NA = 0.75, WD = 4 mm) coupled in a μ-Raman setup (Alpha300, WITec) was applied to find the targeted Ge SBFET and align it with light beam

center by center with the assistance of a CCD camera (DV401-BV, Andor). The overall laser power was corrected by a calibrated photodiode before testing. All these measurements were done at room temperature under ambient conditions and the resulting electrical signals were recorded by a semiconductor analyzer Keysight B1500A.

Acknowledgments

The authors gratefully acknowledge financial support by the Austrian Science Fund (FWF): project No. P29729-N27. The authors further thank the Center for Micro- and Nanostructures for providing the cleanroom facilities. Zehao Song acknowledges financial support from the China Scholarship Council (CSC. 201908420216).

Data availability statement

All data that support the findings of this study are included within the article (and any supplementary files).

ORCID iDs

Zehao Song  <https://orcid.org/0000-0003-3276-7516>
 Masiar Sistani  <https://orcid.org/0000-0001-5730-234X>
 Alois Lugstein  <https://orcid.org/0000-0001-5693-4775>

References

- [1] Fathpour S 2017 Silicon photonics *Handbook of Optoelectronics, Concepts, Devices, and Techniques* 2nd edn (Boca Raton, FL: CRC Press)
- [2] Bogaerts W 2012 Optical Interconnects *Advanced Interconnects for ULSI Technology* (Hoboken, NJ: Wiley) 503–42
- [3] Vivien L *et al* 2007 High speed and high responsivity germanium photodetector integrated in a Silicon-On-Insulator microwaveguide *Opt. Express* **15** 9843–8
- [4] Salamin Y, Ma P, Baeuerle B, Emboras A, Fedoryshyn Y, Heni W, Cheng B, Josten A and Leuthold J 2018 100 GHz plasmonic photodetector *ACS Photon.* **5** 3291–7
- [5] Das U K and Bhattacharyya T K 2020 Opportunities in device scaling for 3 nm Node and beyond: FinFET Versus GAA-FET Versus UFET *IEEE Trans. Electron Devices* **67** 2633–8
- [6] Milazzo A C *et al* 2005 Active pixel sensor array as a detector for electron microscopy *Ultramicroscopy* **104** 152–9
- [7] Ghayour R and Bakhtazad A 1998 Trade-off between speed and efficiency of silicon metal-i-n photodetectors *Solid. State Electron.* **42** 715–20
- [8] Ziebell M, Marris-Morini D, Rasigade G, Fédéli J-M, Crozat P, Cassan E, Bouville D and Vivien L 2012 40 Gbit/s low-loss silicon optical modulator based on a pipin diode *Opt. Express* **20** 10591
- [9] Laux E, Genet C, Skauli T and Ebbesen T W 2008 Plasmonic photon sorters for spectral and polarimetric imaging *Nat. Photon.* **2** 161–4

- [10] White J S, Veronis G, Yu Z, Barnard E S, Chandran A, Fan S and Brongersma M L 2009 Extraordinary optical absorption through subwavelength slits *Opt. Lett.* **34** 686–8
- [11] Tang L, Kocabas S E, Latif S, Okyay A K, Ly-Gagnon D S, Saraswat K C and Miller D A B 2008 Nanometre-scale germanium photodetector enhanced by a near-infrared dipole antenna *Nat. Photon.* **2** 226–9
- [12] Fan P, Huang K C Y, Cao L and Brongersma M L 2013 Redesigning photodetector electrodes as an optical antenna *Nano Lett.* **13** 392–6
- [13] Huang Y, Liu X, Liu Y, Shao Y, Zhang S, Fang C, Han G, Zhang J and Hao Y 2019 Nanostructured multiple-layer black phosphorus photodetector based on localized surface plasmon resonance *Opt. Mater. Express* **9** 739–50
- [14] Lodari M, Biagioni P, Ortolani M, Baldassarre L, Isella G and Bollani M 2019 Plasmon-enhanced Ge-based metal-semiconductor-metal photodetector at near-IR wavelengths *Opt. Express* **27** 20516–24
- [15] Ghosh A, Guha P, Mukherjee S, Bar R, Ray S K and Satyam P V 2016 Growth of Au capped GeO₂ nanowires for visible-light photodetection *Appl. Phys. Lett.* **109** 123105
- [16] Zheng B Y, Wang Y, Nordlander P and Halas N J 2014 Color-selective and CMOS-compatible photodetection based on aluminum plasmonics *Adv. Mater.* **26** 6318–23
- [17] Kral S, Zeiner C, Stöger-Pollach M, Bertagnolli E, Den Hertog M I, Lopez-Haro M, Robin E, El Hajraoui K and Lugstein A 2015 Abrupt Schottky junctions in Al/Ge nanowire heterostructures *Nano Lett.* **15** 4783–7
- [18] Wind L, Sistani M, Song Z, Maeder X, Pohl D, Michler J, Rellinghaus B, Weber W M and Lugstein A 2021 Monolithic metal–semiconductor–metal heterostructures enabling next-generation germanium nanodevices *ACS Appl. Mater. Interfaces* **13** 12393–9
- [19] Staudinger P, Sistani M, Greil J, Bertagnolli E and Lugstein A 2018 Ultrascaled germanium nanowires for highly sensitive photodetection at the quantum ballistic limit *Nano Lett.* **18** 5030–5
- [20] Sistani M, Staudinger P and Lugstein A 2020 Polarity control in Ge nanowires by electronic surface doping *J. Phys. Chem. C* **124** 19858–63
- [21] Wang D, Chang Y L, Wang Q, Cao J, Farmer D B, Gordon R G and Dai H 2004 Surface chemistry and electrical properties of germanium nanowires *J. Am. Chem. Soc.* **126** 11602–11
- [22] Yu K, Yang F, Cong H, Zhou L, Liu Q, Zhang L, Cheng B, Xue C, Zuo Y and Li C 2018 Fabrication of high-hole-mobility germanium-on-insulator wafers through an easy method *J. Alloys Compd.* **750** 182–8
- [23] Furchi M M, Polyushkin D K, Pospischil A and Mueller T 2014 Mechanisms of photoconductivity in atomically thin MoS₂ *Nano Lett.* **14** 6165–70
- [24] Wei P-C, Chattopadhyay S, Yang M-D, Tong S-C, Shen J-L, Lu C-Y, Shih H-C, Chen L-C and Chen K-H 2010 Room-temperature negative photoconductivity in degenerate InN thin films with a supergap excitation *Phys. Rev. B* **81** 045306
- [25] Yang Y, Peng X, Kim H S, Kim T, Jeon S, Kang H K, Choi W, Song J, Doh Y J and Yu D 2015 Hot carrier trapping induced negative photoconductance in InAs nanowires toward novel nonvolatile memory *Nano Lett.* **15** 5875–82
- [26] Baek E, Rim T, Schütt J, Baek C K, Kim K, Baraban L and Cuniberti G 2017 Negative photoconductance in heavily doped Si nanowire field-effect transistors *Nano Lett.* **17** 6727–34
- [27] Yang Y, Li J, Choi S, Jeon S, Cho J H, Lee B H and Lee S 2021 High-responsivity PtSe₂ photodetector enhanced by photogating effect *Appl. Phys. Lett.* **118** 013103
- [28] Zürich M et al 2017 Direct and simultaneous observation of ultrafast electron and hole dynamics in germanium *Nat. Commun.* **8** 15734
- [29] Kingston R H 1956 Review of germanium surface phenomena *J. Appl. Phys.* **27** 101
- [30] Lindley D H and Banbury P C 1960 Surface relaxation effects in germanium at reduced temperatures *J. Phys. Chem. Solids* **14** 200–7
- [31] Ioffe Institute Electrical properties of Germanium (Ge) (<http://www.ioffe.ru/SVA/NSM/Semicond/Ge/electric.html>)
- [32] Gaubas E and Vanhellemont J 2006 Dependence of carrier lifetime in germanium on resistivity and carrier injection level *Appl. Phys. Lett.* **89** 142106
- [33] Schuller J A, Barnard E S, Cai W, Jun Y C, White J S and Brongersma M L 2010 Plasmonics for extreme light concentration and manipulation *Nat. Mater.* **9** 193–204
- [34] Bird G R and Parrish M 1960 The wire grid as a near-infrared polarizer *J. Opt. Soc. Am.* **50** 886–91
- [35] Auton J P 1967 Infrared transmission polarizers by photolithography *Appl. Opt.* **6** 1023–7
- [36] Bräuninger H, Kraus H, Dangschat H, Beuermann K P, Predehl P and Trümper J 1979 Fabrication of transmission gratings for use in cosmic x-ray and XUV astronomy *Appl. Opt.* **18** 3502–5
- [37] Sonek G J, Wagner D K and Ballantyne J M 1981 Ultraviolet grating polarizers *J. Vac. Sci. Technol.* **19** 921
- [38] Lochbihler H, Polnau E and Predehl P 1995 Polarimetry of transmission gratings *Appl. Opt.* **34** 5725–31
- [39] Echtermeyer T J, Milana S, Sassi U, Eiden A, Wu M, Lidorikis E and Ferrari A C 2016 Surface plasmon polariton graphene photodetectors *Nano Lett.* **16** 8–20
- [40] Sobhani A, Knight M W, Wang Y, Zheng B, King N S, Brown L V, Fang Z, Nordlander P and Halas N J 2013 Narrowband photodetection in the near-infrared with a plasmon-induced hot electron device *Nat. Commun.* **4** 1643
- [41] Ruda H E and Shik A 2005 Polarization-sensitive optical phenomena in semiconducting and metallic nanowires *Phys. Rev. B* **72** 115308
- [42] Berini P 2009 Long-range surface plasmon polaritons *Adv. Opt. Photon.* **1** 484–588
- [43] Ahn Y H and Park J 2007 Efficient visible light detection using individual germanium nanowire field effect transistors *Appl. Phys. Lett.* **91** 162102
- [44] Mukherjee S, Das K, Das S and Ray S K 2018 Highly responsive, polarization sensitive, self-biased single GeO₂-Ge nanowire device for broadband and low power photodetectors *ACS Photon.* **5** 4170–8